



HAL
open science

Phase diagram of a three-dimensional dipolar model on an fcc lattice

Vincent Russier, Juan J Alonso, I Lisiecki, A T Ngo, C Salzemann, S Nakamae, C Raepsaet

► **To cite this version:**

Vincent Russier, Juan J Alonso, I Lisiecki, A T Ngo, C Salzemann, et al.. Phase diagram of a three-dimensional dipolar model on an fcc lattice. *Physical Review B*, 2020, 102, 10.1103/PhysRevB.102.174410 . hal-03000085

HAL Id: hal-03000085

<https://hal.science/hal-03000085>

Submitted on 11 Nov 2020

HAL is a multi-disciplinary open access archive for the deposit and dissemination of scientific research documents, whether they are published or not. The documents may come from teaching and research institutions in France or abroad, or from public or private research centers.

L'archive ouverte pluridisciplinaire **HAL**, est destinée au dépôt et à la diffusion de documents scientifiques de niveau recherche, publiés ou non, émanant des établissements d'enseignement et de recherche français ou étrangers, des laboratoires publics ou privés.

Phase diagram of a three-dimensional dipolar model on an fcc lattice.

V. Russier,^{1,*} Juan J. Alonso,^{2,3,†} I. Lisiecki,⁴ A.T. Ngo,⁴ C. Salzemann,⁴ S. Nakamae,⁵ and C. Raepsaet⁵

¹*ICMPE, UMR 7182 CNRS and UPE 2-8 rue Henri Dunant 94320 Thiais, France.*

²*Física Aplicada I, Universidad de Málaga, 29071 Málaga, Spain*

³*Instituto Carlos I de Física Teórica y Computacional, Universidad de Málaga, 29071 Málaga, Spain*

⁴*Sorbonne Université, CNRS, UMR 8233 De la Molécule aux Nano-Objets: Réactivité, Interactions Spectroscopies, MONARIS, 75005, Paris, France*

⁵*CEA/DRF/IRAMIS/SPEC and CNRS UMR 3680, 91191, Gf sur Yvette, France*

(Dated: November 11, 2020)

The magnetic phase diagram at zero external field of an ensemble of dipoles with uniaxial anisotropy on a FCC lattice is investigated from tempered Monte Carlo simulations. The uniaxial anisotropy is characterized by a random distribution of easy axes and its magnitude λ_u is the driving force of disorder and consequently frustration. The phase diagram, separating the paramagnetic, ferromagnetic, quasi long range ordered ferromagnetic and spin-glass regions is thus considered in the temperature, λ_u plane. This system is aimed at modeling the magnetic phase diagram of supracrystals of magnetic nanoparticles.

DOI: 10.1103/PhysRevB.102.174410

arXiv:2011.00879v2 [cond-mat.mtrl-sci] 10 Nov 2020

* e-mail address: russier@icmpe.cnrs.fr

† e-mail address: jjalonso@uma.es

I. INTRODUCTION

Assembly of magnetic nanoparticles (MNP) in dense packed structures receives a growing interest as a way to build new composite materials in a bottom-up strategy. Besides promising applications, for instance in nanomedicine¹ inductor nanotechnology², or mechanical properties^{3,4}, the MNP dense packed assemblies present a great fundamental interest both in nanoscale magnetism^{5,6}, because of collective effects leading among others to complex magnetic phases, and for the knowledge of self organization process.

Among the diverse dense packed MNP assemblies synthesized experimentally one can distinguish the random packed ones from the long range well ordered 2D or 3D supra-crystals, namely periodic crystals of MNP. Examples of the former are the discontinuous metal-insulator multilayers (DMIM) of CoFe in alumina matrix^{7,8} or pellets made of pressed bare iron oxide MNP reaching the random close packed volume fraction limit^{9,10}. The latter involve MNP assemblies with well controlled size and shape and strongly reduced polydispersity on the first hand and the control of the organization, or self-organization process on the other hand. Slow evaporation and/or solvent destabilization of colloid suspensions, are good examples of quite efficient methods to get well ordered supra-crystals. Following this route, ensembles of nearly spherical MNP characterized by a strongly reduced polydispersity and coated with an organic layer preventing nanoparticle agglomeration self organize according to hard sphere like rules in dense packed structures of either body centered tetragonal (BCT), hexagonal close packed (HCP) or face centered cubic (FCC) symmetry^{3,4,11}. Similarly, the alternative method based upon a protein crystallization technique, leads to long range well organized FCC supra-crystals of iron oxide MNP free of direct contact owing to the protein cage¹²⁻¹⁴. Hence, cobalt or iron oxide MNP long range supra-crystals with FCC or HCP structure are currently available experimentally. These supra-crystals quite generally made of nanoparticles coated by a non magnetic layer are characterized by a resulting volume fraction of the magnetic cores typically in between 0.30 to 0.75 times the maximum value for particles at contact on the corresponding lattice. In the range of sizes considered, the MNP are single domain and therefore bear a large moment referred to as superspin (c.a. $2 \cdot 10^4$ to $2 \cdot 10^5 \mu_B$ for iron oxide MNP of 10 to 20 nm in diameter). As a result, in these assemblies the mean dipole interaction between MNP taking into account the volume fraction E_d/k_B reaches up to 100 to 300 K for iron oxide MNP of diameter ~ 12 nm and up to $3 \cdot 10^3$ K for cobalt MNP of diameter ~ 10 nm. This makes the low temperature magnetic phase likely to be, at least partly, conditioned by dipolar collective behavior, a question which receives a large interest both experimentally¹⁵⁻¹⁷ and theoretically⁸.

The modeling of the magnetic properties of dense packed structures of MNP is in principle a multi scale problem but is fortunately highly simplified for particles whose size falls in the single domain range if the non collinearity of the surface spins is neglected (the so-called spin canting). Then the effective one spin model (EOSM) can be used although this level of approximation has been questioned and extended for situations where the core-surface MNP morphology is expected to play a significant role^{18,19}. In the framework of the EOSM and considering the MNP as frozen in position in the system one is led to model an ensemble of MNP free of super exchange interaction owing to the non magnetic coating layer and thus interacting only through the dipole dipole interaction (DDI) between the moments of the macro spins and undergoing the magneto-crystalline anisotropy energy (MAE). It is well known that strongly coupled dipolar systems present a low temperature phase dependent on the underlying structure and the amount of disorder²⁰⁻²⁴ which originates either from the structure, the dilution or the MAE through the distribution of easy axes. Hence, the so-called super ferromagnetic (SFM) or super spin-glass (SSG) phases can be observed. Experimental evidence of the SSG state has been given either in randomly distributed MNP or on well ordered MNP supra-crystals with randomly distributed anisotropy easy axes. In the case of well ordered supra-crystals for which a FCC lattice is a representative situation, the low temperature phase results from the competition between the dipolar induced ferromagnetic phase of the purely dipolar system (free of MAE), and the frustration introduced by the disorder. In the case of uniaxial MAE and for a wholly occupied lattice, the latter comes only from either the amplitude of the MAE when the easy axes distribution is random, or the degree of alignment of the easy axes in the

strong MAE limit. The former situation corresponds to a supra-crystal synthesized in the absence of external field. This strong MAE limit has been investigated recently in the random close packed and for MNP on a perfect FCC lattice^{25,26}.

The influence of the random anisotropy such as introduced by the uniaxial MAE with random distribution of easy axes has already been widely studied in the framework of the random anisotropy model (RAM), first introduced by Harris *et al.*²⁷, where the spin-spin interaction is quite generally the short-range Heisenberg or Ising exchange one, the latter being the strong anisotropy limit of the former. The relevant disorder control parameter is the anisotropy to exchange ratio (D/J) which governs the crossover from the FM state ($D/J = 0$) to the spin-glass state obtained in the $D/J \rightarrow \infty$ limit²⁸, where D and J are the anisotropy and exchange coupling constants respectively. When D/J increases the long-range (LR) FM state first disorders to a quasi long-range order (QLRO) state with a ferromagnetic character²⁹. The Monte Carlo simulations of Nguyen and Hsiao^{30,31} show clearly, on the basis of the dynamic behavior, that the PM/FM like magnetic phase transition at weak anisotropy disappears with the increase of D/J and a glassy phase transition takes place beyond a threshold value. This scenario is also in agreement with the simulation results for the spontaneous magnetization in terms of (D/J) ³².

In the present work following related contributions on the dipolar Ising model^{25,26} devoted to the effect of the MAE easy axes texturation in the infinite MAE limit, we investigate the magnetic phase diagram from Monte Carlo simulations of FCC supra-crystals of MNP interacting *via* DDI and undergoing a uniaxial MAE whose easy axes are randomly distributed. Here the disorder control parameter is the MAE to the DDI strengths ratio as is the case in the RAM. An important difference with the dipolar Ising model studied in Refs.^{25,26} is the 3 dimensional nature of the model variables, as is the case in the Heisenberg model with important consequences essentially in the spin-glass phase and with the occurrence of a transverse spin-glass state associated with a QLRO in the FM region of the phase diagram. The choice of the FCC structure is mainly dictated by the MNP organizations obtained experimentally as outlined above. To investigate the phase diagram we calculate the ferromagnetic and overlap spin-glass order parameters, from which a finite size analysis of the corresponding Binder cumulants, spin-glass and transverse spin-glass correlation lengths is performed. We also focus on the finite size behavior of the heat capacity. The paper is organized as follows. We introduce the model in section II, the simulation details and the observables we use are then presented in section II A and II B respectively. Section III is devoted to the analysis of the results and a conclusion is given in section IV.

II. MODEL

We model an assembly of MNP free of super exchange interactions, characterized by a uniaxial magneto-crystalline anisotropy (MAE) and self organized on a supra-crystal of face centered cubic (FCC) structure. To this aim we place ourselves in the framework of the effective one spin model where each single domain MNP is assumed to be uniformly magnetized with a temperature independent saturation magnetization M_s . Hence we consider a system of N dipolar hard spheres of moment $\vec{\mu}_i = \mu \hat{\mu}_i$ located on the sites of a FCC lattice occupying a total volume V , interacting through the usual dipole dipole interaction (DDI) and subjected to a one-body anisotropy energy, $-K_i v_i (\hat{n}_i \cdot \hat{\mu}_i)^2$. $\hat{\mu}_i$ and \hat{n}_i are three dimensional unit vectors and in the following, hatted letters denote unit vectors. K_i , \hat{n}_i and v_i are the anisotropy constant, the easy axis and the volume of the particle i respectively. We consider a random distribution of easy axes on the unit sphere, namely the azimuthal angles are randomly chosen while the polar angle distribution follow the probability density $\sin(\Theta)/2$. The MNP ensemble is monodisperse with MNP diameter d . The particle moment is related to the material saturation magnetization M_s through $\mu = v(d)M_s$ ($v(d) = \pi d^3/6$). The

Hamiltonian of the system is given by

$$\beta H = \frac{1}{2} \beta \epsilon_d \sum_{i \neq j} \frac{\hat{\mu}_i \cdot \hat{\mu}_j - 3(\hat{\mu}_i \cdot \hat{r}_{ij})(\hat{\mu}_j \cdot \hat{r}_{ij})}{(r_{ij}/d)^3} - \beta K v(d) \sum_i (\hat{n}_i \cdot \hat{\mu}_i)^2 \quad \text{with } \epsilon_d = \frac{\mu_0 \mu^2}{4\pi d^3} \quad (1)$$

where \hat{r}_{ij} is the unit vector carried by the vector joining sites i and j , r_{ij} its length and $\beta = 1/(k_B T)$ is the inverse temperature. The Hamiltonian (1) is the same as that used in²⁴ while in²⁵, where the infinite anisotropy limit was considered, the second term of equation (1) was not included and the directions of the moments, $\hat{\mu}_i$ were set equal to the easy axes \hat{n}_i representing then the Ising axes. Concerning the reduced temperature, instead of the natural choice $T k_B / \epsilon_d$, we take advantage of the $1/r^3$ dependence of the DDI to introduce the more convenient reduced temperature $T^* = T k_B / (\epsilon_d (d/d_r)^3)$, with $d_r = d(\Phi_r/\Phi)^{1/3}$ where Φ and Φ_r are respectively the volume fraction, $(N/V)\pi d^3/6$, and a reference value (here, the maximum value for hard spheres on a FCC lattice). This choice of T^* equivalent to measuring the temperature in terms of a dipole dipole energy weighted by the volume fraction instead of its maximum value at contact^{26,33}. Equation (1) is then rewritten as

$$\beta H = \frac{1}{T^*} \left(\frac{1}{2} \sum_{i \neq j} \frac{\hat{\mu}_i \cdot \hat{\mu}_j - 3(\hat{\mu}_i \cdot \hat{r}_{ij})(\hat{\mu}_j \cdot \hat{r}_{ij})}{(r_{ij}/d_r)^3} - \lambda_u \sum_i (\hat{n}_i \cdot \hat{\mu}_i)^2 \right) \quad \lambda_u = \frac{K v(d)}{\epsilon_d} (d_r/d)^3 \quad (2a)$$

$$\equiv \frac{1}{T^*} \left(\frac{1}{2} \sum_{i \neq j} \hat{\mu}_i \bar{T}_{ij} \hat{\mu}_j - \lambda_u \sum_i (\hat{n}_i \cdot \hat{\mu}_i)^2 \right) \quad (2b)$$

which introduces the MAE coupling constant λ_u .

The simulation box is a cube with edge length $L_s = \sqrt{2} L d_r$ and the total number of dipoles is $N = 4L^3$. (In the following without loss of generality we consider the case of a FCC lattice with $d_r = d$). We consider periodic boundary conditions by repeating the simulation cubic box identically in the 3 dimensions. The long range DDI interaction is treated through the Ewald summation technique^{21,34}, with a cut-off $k_c = 10 k_m$, $k_m = (2\pi/L_s)$, in the sum of reciprocal space and the α parameter of the direct sum chosen is $\alpha = 5.80$, a value which permits to limit the sum in direct space to the first image term^{21,35}. The Ewald sums are performed with the so-called conductive external conditions^{21,34}, i.e. the system is embedded in a medium with infinite permeability, $\mu_s = \infty$, which is a way to avoid the demagnetizing effect and thus to simulate the intrinsic bulk material properties regardless of the external surface and system shape effects. For the different values of λ_u considered in the following, the simulations are performed for system sizes up to either $L = 7$ ($N = 1372$) or $L = 8$ ($N = 2048$).

A. Simulation method

In order to thermalize in an efficient way our system presenting strongly frustrated states, we use parallel tempering algorithm^{36,37} (also called tempered Monte Carlo) for our Monte Carlo simulations. Such a scheme is widely used in similar systems^{25,26,38}, and we do not provide the details. The method is based on the simultaneous simulation runs of identical replica for a set of temperatures $\{T_n^*\}$ with exchange trials of the configurations pertaining to different temperatures each N_M Metropolis steps according to an exchange rule satisfying the detailed balance condition. The set of temperatures is chosen in such a way that it brackets the transition temperature while ensuring a satisfying rate of exchange between adjacent temperature configurations. Our set $\{T_n^*\}$ is either an arithmetic distribution or an optimized one in order to make the exchange rate between adjacent paths as constant as possible in the whole range of $\{T_n^*\}$ according to the efficient constant entropy increase method³⁹. In the present work we take $N_M = 10$, the number of temperatures is in between 36 and 48 according to the value of L and the amplitude of temperatures in the set $\{T_n^*\}$ for $L \leq 7$ and up to 96 for $L = 8$. When necessary, precise interpolation for temperatures between

the points actually simulated are done through reweighting methods⁴⁰. We use t_0 Monte Carlo steps (MCS) for the thermalization and the averaging is performed over the $(t_0, 2t_0)$ interval following MCS with $t_0 = 5 \cdot 10^5$.

We deal with frozen disorder situations where each realization of the easy axes distribution $\{\hat{n}_i\}$ defines a sample. Accordingly, a double averaging process is performed first relative to the thermal activation, *i.e.* the Monte Carlo step, and second on the whole set of N_s samples. Consequently, the mean value of an observable A , results from a double averaging denoted in the following as $[\langle A \rangle]$ where $\langle . \rangle$ corresponds to the thermal average on the MC sampling for a fixed realization of the axes distribution and $[.]$ to the average over the set of samples considered. The number of samples necessary to get an accurate result depends strongly on the value of λ_u . Obviously, for $\lambda_u = 0$, $N_s = 1$ should be sufficient for a very long MC run in order to get a satisfying average. In practice, we use $N_s = 10$ for $\lambda_u = 0$. We find that N_s of the order of 100 to 200 is sufficient up to $\lambda_u \leq 1.5$ whereas accurate results for $\lambda_u = 4$ require the use of at least $N_s = 400$ realizations. However, it is worth mentioning that accurate results for the heat capacity C_v are much less demanding than for the overlap order parameter and about 50 to 100 realizations allow to get very well averaged C_v up to $\lambda_u = 100$. In any case, in the present work we limit ourselves to $\lambda_u = 4$ in the computations of the spin-glass overlap order parameter q_2 and related properties. The error bars of the averaged quantities are deduced from the mean squared deviations of the sample to sample fluctuations. The simulation code is massively parallelized, all temperatures and the 2 replicas running together, and the typical CPU time is *c.a.* 40h for the complete run of one sample of $L = 7$ ($N = 1372$) on the Intel Xeon E5 processors at the CINES center.

B. Observables

Our main purpose is the determination of the transition temperature between the paramagnetic and the ordered phase and on the nature of the latter, namely ferromagnetic or spin-glass, in terms of λ_u . For the PM/FM transition, we consider the spontaneous magnetization

$$m = \frac{1}{N} \left\| \sum_i \hat{\mu}_i \right\| \quad (3)$$

computing its moments, $m_n = [\langle m^n \rangle]$, $n = 1, 2$ and 4. We compute also the nematic order parameter P_2 together with the instantaneous nematic direction, \hat{d} which are the largest eigenvalue and the corresponding eigenvector respectively of the tensor $\bar{Q} = \frac{1}{N} \sum_i (3\hat{\mu}_i \hat{\mu}_i - \bar{I})/2$ ²¹, where \bar{I} is the unit tensor of cartesian components $I_{\alpha\beta} = \delta_{\alpha\beta}$. The spontaneous magnetization can also be studied in the ordered phase from the mean value projected total magnetization on the nematic direction, which defines

$$m_d = \frac{1}{N} \sum_i \hat{\mu}_i \cdot \hat{d} \quad (4)$$

We compute the mean value $m_{d1} = [\langle |m_d| \rangle]$ and the moments $m_{dn} = [\langle m_d^n \rangle]$, with $n = 2, 4$. To locate the transition temperature, T_c^* , as usually done, we will use the finite size scaling (FSS) analysis of the Binder cumulant⁴¹ which is defined either from the moments m_n or m_{dn} characterized by 3 or one degree of freedom respectively

$$B_m = \frac{1}{2} \left(5 - 3 \frac{m_4}{m_2^2} \right), \quad B_{md} = \frac{1}{2} \left(3 - \frac{m_{d4}}{m_{d2}^2} \right) \quad (5)$$

From these normalizations, $B_m, B_{md} \rightarrow 1$ in the long range FM phase and $B_m, B_{md} \rightarrow 0$ in the limit $L \rightarrow \infty$ in the disordered PM phase. For the PM/SG transition, we consider the usual overlap order parameter^{42,43}

$$q^2 = \sum_{\alpha\beta} |q_{\alpha\beta}|^2, \quad \text{with} \quad q_{\alpha\beta} = \frac{1}{N} \sum_i \mu_{i\alpha}^{(1)} \mu_{i\beta}^{(2)}, \quad (6)$$

where the superscripts ⁽¹⁾ and ⁽²⁾ stand for two independent replicas of an identical sample and α, β denote the cartesian coordinates. From q^2 we calculate the mean value $q_2 = [\langle |q^2| \rangle]$ and $q_4 = [\langle q^4 \rangle]$ and the corresponding Binder cumulant,

$$B_q = \frac{1}{2} \left(11 - 9 \frac{q_4}{q_2^2} \right) \quad (7)$$

In order to determine the PM/SG transition temperature it may be more convenient to use the spin-glass correlation length, usually defined from a fit of the spin-glass overlap parameter correlation function on its Ornstein-Zernike form, assuming that it follows from a so called Φ^4 theory^{44,45}

$$\xi = \frac{1}{2 \sin(k_m/2)} \left(\frac{q_2(0)}{q_2(\vec{k}_m)} - 1 \right)^{1/2} \quad \text{with} \quad q_2(\vec{k}) = \left\langle \left[\sum_{\alpha, \beta} q_{\alpha\beta}(\vec{k}) q_{\alpha\beta}^*(\vec{k}) \right] \right\rangle \quad q_{\alpha\beta}(\vec{k}) = \frac{1}{N} \sum_i \mu_{i\alpha}^{(1)} \mu_{i\beta}^{(2)} e^{i\vec{k}\vec{r}_i}, \quad (8)$$

with $\vec{k}_m = (k_m, 0, 0)$. By exploiting the non dimensional character of the ratio ξ/L one is led to deduce T_c^* as the crossing point of the ξ/L curves in terms of T^* for different values of L . Finally, the magnetic susceptibility, χ_m and the heat capacity, C_v are calculated from the magnetization and the energy fluctuations respectively

$$\chi_m = \frac{N}{T^*} [\langle m^2 \rangle - \langle m \rangle^2] \quad , \quad C_v = \frac{1}{NT^{*2}} [\langle H^2 \rangle - \langle H \rangle^2] \quad (9)$$

III. RESULTS

The phase diagram, which summarizes the present work, is displayed in figure (1). It separates the paramagnetic (PM), ferromagnetic (FM) and the spin-glass (SG) phases. The important feature of $T_c^*(\lambda_u)$ along both the PM/FM and the PM/SG lines is its very weak dependency with λ_u , the overall variation being limited to $0.6 \leq T_c^* \leq 1.0$.

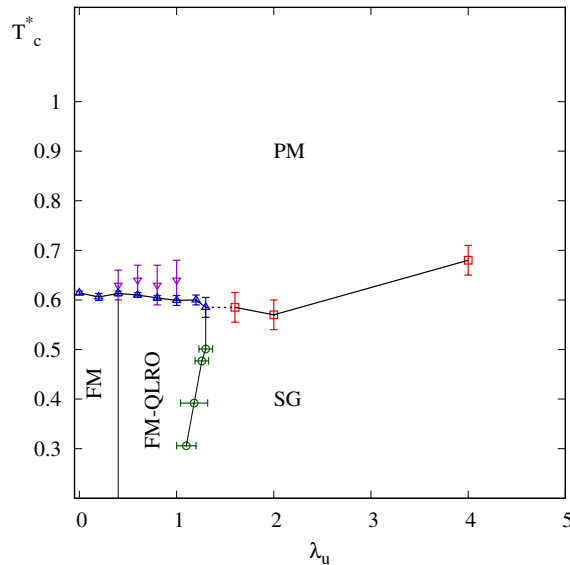


FIG. 1. Phase diagram in the (T^*, λ_u) plane separating the PM, FM, SG regions. We also indicate the estimated range in λ_u corresponding to the FM-QLRO and transverse spin-glass phase. Open upward triangles: PM/FM line; open squares: PM/SG line; open downward triangles: transverse spin-glass transition temperature, T_{xy} ; open circles: FM/SG line obtained from the behavior of B_m in terms of L at constant T^* .

Before going in the details of its determination, a qualitative overview of the evolution with respect to the MAE coupling constant λ_u combined with the finite size effect of both the ferromagnetic and nematic order parameters, namely the magnetization m and the eigenvalue P_2 is useful. This is displayed in figure (2). The rising of the nematic

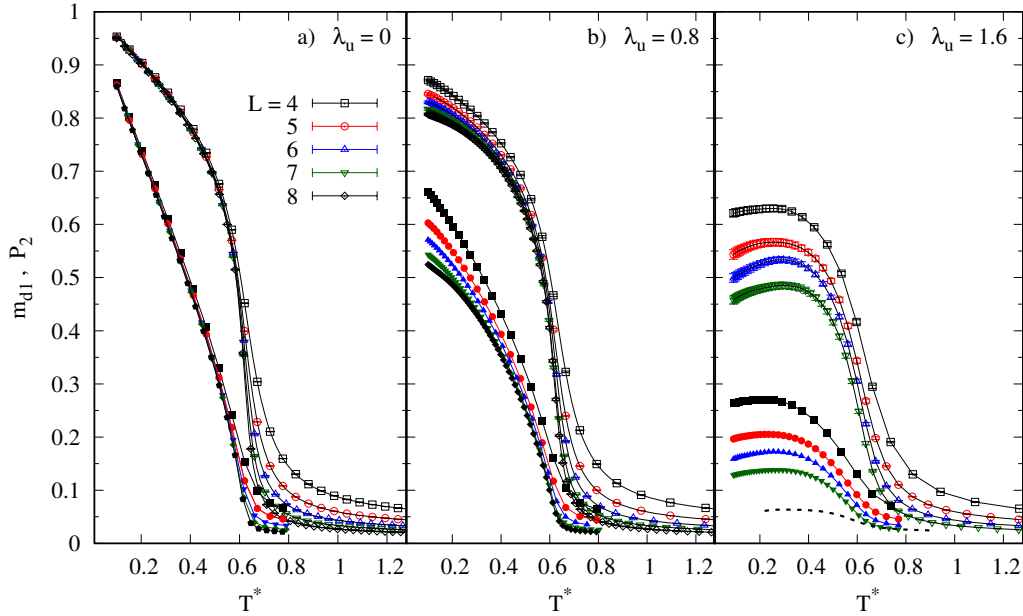


FIG. 2. Polarization m_{d1} , open symbols and nematic order parameter, [$\langle P_2 \rangle$] solid symbols in terms of T^* for a) $\lambda_u = 0$, b) $\lambda_u = 0.8$ and c) $\lambda_u = 1.6$ for different system sizes $L = 4$ to 8 ($N = 256$ to 2048) for $\lambda_u = 0$ and 0.8 , and $L = 4$ to 7 for $\lambda_u = 1.6$, as indicated. In c) the dashed line represents P_2 for $\lambda_u = 2$ and $L = 7$ to illustrate the gradual vanishing of the nematic order at low T^* with the increase of λ_u . The lines result from the interpolation performed by the reweighting method⁴⁰.

order parameter below a threshold temperature, close to the transition temperature T_c^* is indicative of the occurrence of a collective spontaneous direction in the system induced by the DDI which competes with the random anisotropy contribution. It is worth mentioning that the finite value of the order parameters in the PM phase, well above T_c^* , results from the short range correlations in finite size systems²⁹ and is a quite general result^{22,23,46,47}. The curves of figure (2) suggest clearly an evolution of the low temperature phase from a well ordered FM phase in figure (2 a) corresponding to the pure dipolar case, $\lambda_u = 0$ where the PM/FM transition is well established^{20,21,24,47} to a gradual crossover to the absence of FM order, figure (2 c) with the complete disappearance of the latter at $\lambda_u = 2$. Between these two regimes, figure (2 b), the similarity of m and P_2 in terms of T^* with the pure dipolar case remains only on a qualitative level since then both order parameters P_2 and m decrease with the system size L conversely to the case at $\lambda_u = 0$. The behavior of both P_2 and m at $\lambda_u = 0.2$ is characterized, as is the case at $\lambda_u = 0$ by the merging at low T^* of the curves corresponding to different values of L , indicating a finite value of P_2 and m in the thermodynamic limit ($L \rightarrow \infty$) and we find the onset of the decrease with L of the ferromagnetic order parameters at $\lambda_u \simeq 0.4$, as is clarified in figure (3c) where we compare the behavior of $m_2(T^*)$ with the system size between $\lambda_u = 0.4$ and 0.8 .

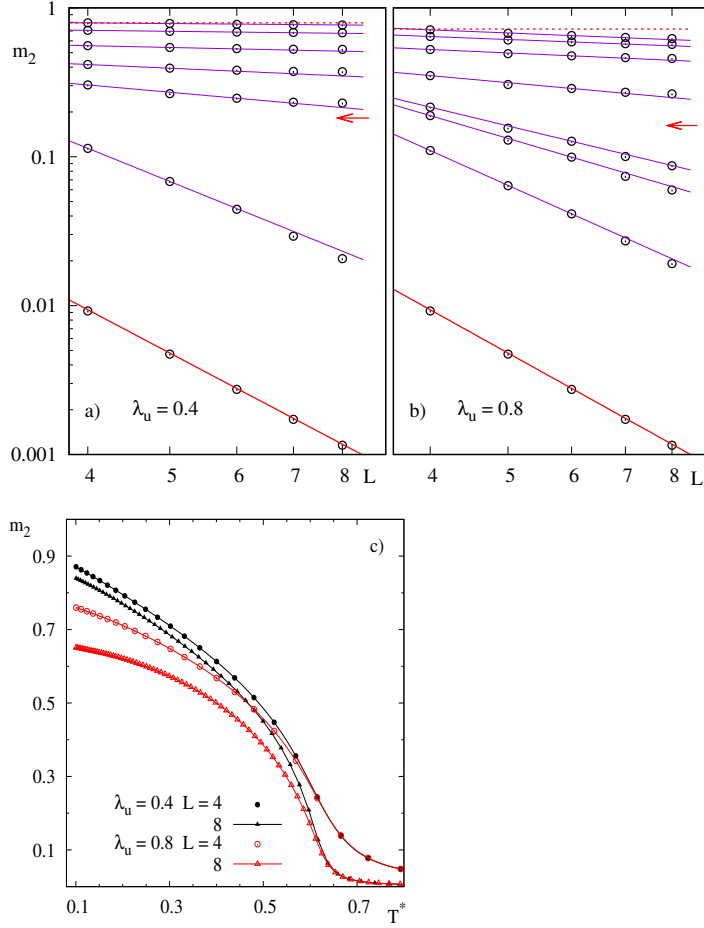


FIG. 3. Log-log plot of m_2 in terms of L for : a) $\lambda_u = 0.4$ and $T^* = 0.2028, 0.3050, 0.4481, 0.5402, 0.5913, 0.6833, 1.910$ from top to bottom; b) $\lambda_u = 0.8$ and $T^* = 0.1983, 0.3084, 0.4429, 0.5651, 0.6263, 0.6385, 0.6874, 1.9100$. The dotted lines are guides to the eyes for $m_2 = \text{const}$. at the smallest temperature; the solid lines are linear interpolation determined from $L = 4$ and $L = 6$. excepted at bottom where they indicates the $1/L^3$ behavior in the PM phase. The arrow localizes T_c^* . c) m_2 in terms of T^* for $\lambda_u = 0.4$ at $L = 4$ and 8 ($N = 256$ and 2048) compared to the case $\lambda_u = 0.8$ which shows the onset at $\lambda_u = 0.4$ of the decrease of m_2 with respect to L at low temperature. Error bars in all panels are smaller than the size of the symbols.

A. Ferromagnetic transition

For small values of λ_u , starting from $\lambda_u = 0$, we check the ferromagnetic nature of the low temperature phase and determine the transition temperature T_c^* by following the FSS and thus we look for the crossing point of the Binder cumulant, $B_m(L)$ curves for different values of L , consequence of the scaling behavior

$$B_m = b_m((T^* - T_c^*)L^{1/\nu}) . \quad (10)$$

However, the system sizes considered in the present work are too small to determine accurate values of the exponent ν . At $\lambda_u = 0$ we get $T_c^* = 0.614 \pm 0.004$ in agreement with Refs.^{20,24,47}. The spontaneous magnetization orientates along the $\langle 111 \rangle$ directions in agreement with results of the literature^{20,47} and as Alkadour *et al.*⁴⁷ we do not find any spin reorientation at low temperature. Moreover we have checked that equation (10) is very well reproduced using $\nu = 0.692$ ⁴⁸, the value of ν obtained for dipoles on lattice of cubic symmetry from renormalization group developments, (see figure (4 a,b)). Another important feature of the PM/FM transition is the strong finite size dependence of both the heat capacity C_v and the magnetic susceptibility χ_m with a peak located at $T_L^*(A)$, ($A = C_v, \chi_m$), and $T_L^*(A) \rightarrow T_c^*$ in the $L \rightarrow \infty$ limit^{26,49}. This behavior, leading to a divergence of χ_m (not shown) at T_c is displayed on figure (5a) for C_v ⁵⁰.

When λ_u increases in the low MAE regime, the behavior of m_2 with respect to the system size changes as we observe a decrease of the magnetization with the increase of L at low temperature (see figure (2 b)). Although we cannot rule out a crossover for much larger values of L leading to a convergence of $m(T^*)$ at fixed and low T^* we interpret this behavior as a FM state with quasi long range order with $m(L \rightarrow \infty) = 0$ well below T_c^* , instead of a long range FM one. In the absence of MAE, the different $m(L, T^*)$ merge at low T^* (see figure (2 a) and Ref.²⁴) which is no longer the case beyond $\lambda_u \sim 0.4$ as can be seen in figures (2 b) and (3 c). This FM-QLRO is observed beyond $\lambda_u \simeq 0.4$ as shown in figure (3) where m_2 in terms of L in log scale (a and b) and m_2 in terms of T^* for different values of L (c) are displayed for $\lambda_u = 0.4$ and 0.8. In any case the paramagnetic behavior, namely $m_2 \sim 1/N$, is reached sufficiently far from T_c^* . The FM-QLRO is related to the onset of the transverse spin-glass state⁵¹ where the components of the moments normal to the nematic direction freeze in a spin-glass like state and corresponds to the mixed state of the phase diagram outlined by Ayton *et al.*²². The transverse spin-glass state is defined in the FM region of the phase diagram and characterized by the transverse overlap order parameter, q_{2t} , obtained by using the transverse components $\hat{\mu}_{it} = (\hat{\mu}_i - (\hat{d} \cdot \hat{\mu}_i)\hat{d}) / \left\| (\hat{\mu}_i - (\hat{d} \cdot \hat{\mu}_i)\hat{d}) \right\|$ of the moments instead of $\hat{\mu}_i$ in equation (6). From the behavior of q_{2t} in terms of T^* , given in figure (6 a) for increasing values of λ_u , we see that no transverse spin-glass state is expected for $\lambda_u < 0.4$. Indeed, q_{2t} not only remains very small on the whole range of T^* but presents no noticeable rising up at low temperature and is moreover a decreasing function of L down to very low temperature up to $\lambda_u = 0.35$ as shown in figure (6 b,c) where we also compare figure (6 d) to the case $\lambda_u = 0.8$ well inside the FM-QLRO region of the phase diagram. We emphasize that this is related to the onset at $\lambda_u = 0.4$ of the the L -dependence of $m_2(T^*)$ at low T^* as mentioned above. Given the very small values taken by q_{2t} for $\lambda_u = 0.35$, we cannot interpret the crossing point of the $q_{2t}(T^*)$ curves for different values of L as the onset of the transverse spin-glass state. We emphasize that $q_{2t}(T^*)$ when $T^* < 0.6$ remains smaller or comparable to its value at the hump ($\sqrt{q_{2t}} \leq 0.04 \ll 1$). This is no longer the case for instance at $\lambda_u = 0.8$, figure (6a, d), in the FM-QLRO region of the phase diagram. The corresponding transition temperature, T_{xy}^* below which the FM and transverse spin-glass orders coexist is determined by the crossing point of the ξ_t/L curves where ξ_t is the transverse spin-glass correlation length as obtained from equation (8) with the overlap order parameter replaced by its transverse equivalent. The result we get is that T_{xy}^* is very close to and seems slightly larger than the PM/FM transition temperature T_c^* , see figures (7) and (1). The small difference between T_{xy}^* and T_c^* is however not really meaningful given the error bars (see figure (1)). Therefore we are led to conclude from the present simulations that T_{xy}^* and T_c^* are likely to coincide.

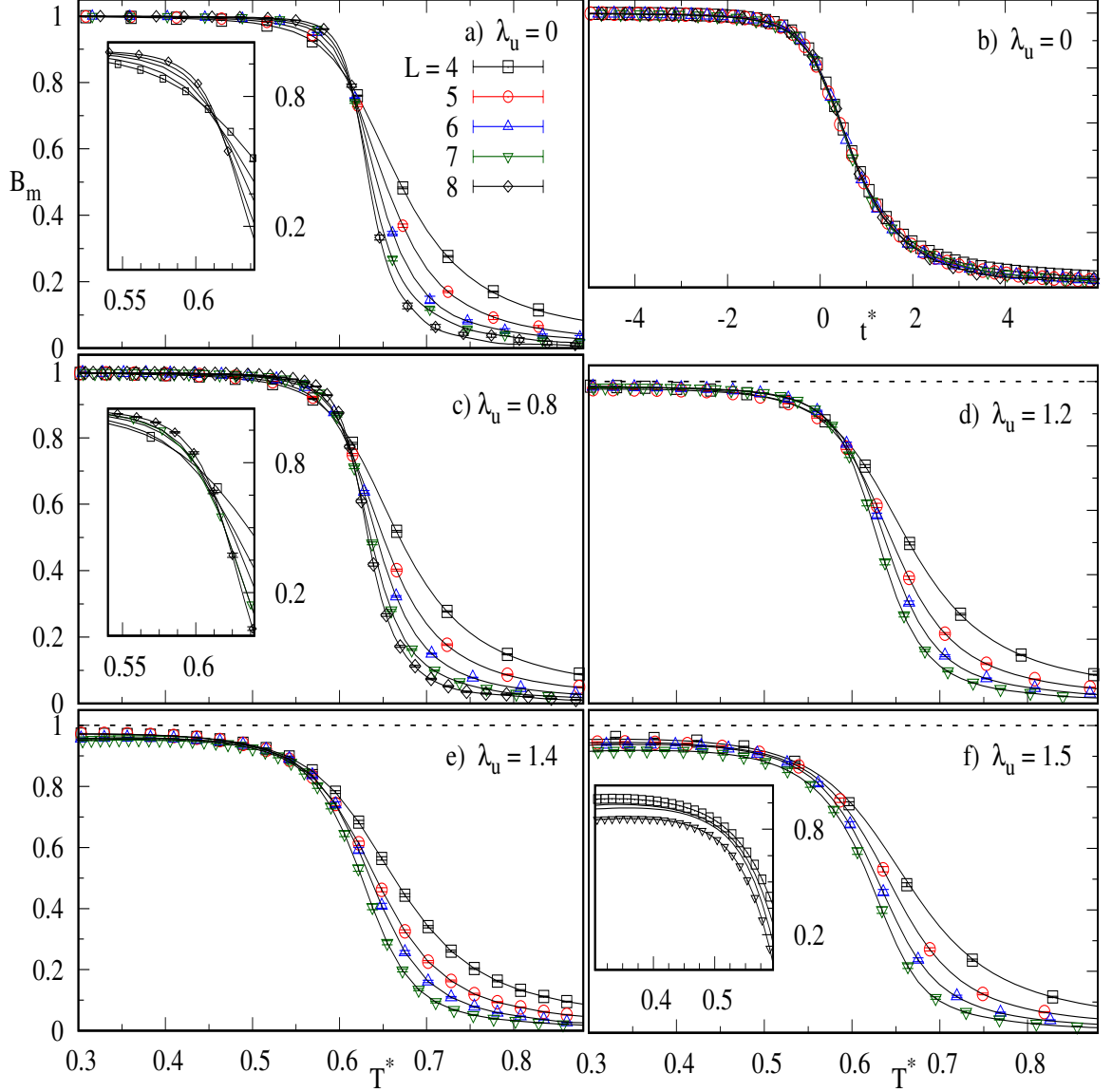


FIG. 4. Magnetization Binder cumulant for different system sizes as indicated. In the pure dipolar case (a) and b)). a) in terms of T^* ; b) rescaled according to equation (10) with $t^* = (T^* - T_c^*)L^{1s/\nu}$, $T_c^* = 0.614$ and $\nu = 0.692^{48}$. For different values of λ_u , as indicated (c) to f)); including the vicinity, $\lambda_u = 1.4$, e) and f) beyond, $\lambda_u = 1.5$, the onset of the SG phase of the magnetic phase diagram. The lines are the interpolations according to the reweighting method⁴⁰. The dotted line in d) to f) is a guide to the $B_m = 1$ limiting value, which is no longer reached for $\lambda_u \geq 1.2$.

Increasing λ_u , we still find a PM/FM transition up to $\lambda_u = 1.3$ as indicated by the behavior of B_m as shown in figure (4 c,d). Indeed, we still get a crossing point in temperature, allowing the determination of T_c^* . Moreover, the orientation of the magnetization in the FM phase remains very close to the $\langle 111 \rangle$ directions (see figure (8b)). Of course the distribution of the moments around the mean polarization direction depends largely on λ_u and this can be easily visualized from an instantaneous moment configuration as is done in figure (8 a,b) and estimated from the variation of the nematic order parameter mean value, P_2 in terms of λ_u at constant temperature. Using a simple model to represent the distribution of the moment around the nematic direction, as for instance $P(\Theta) \propto \sin(\Theta)[\exp(-\Theta^2/(2\sigma^2))]$,

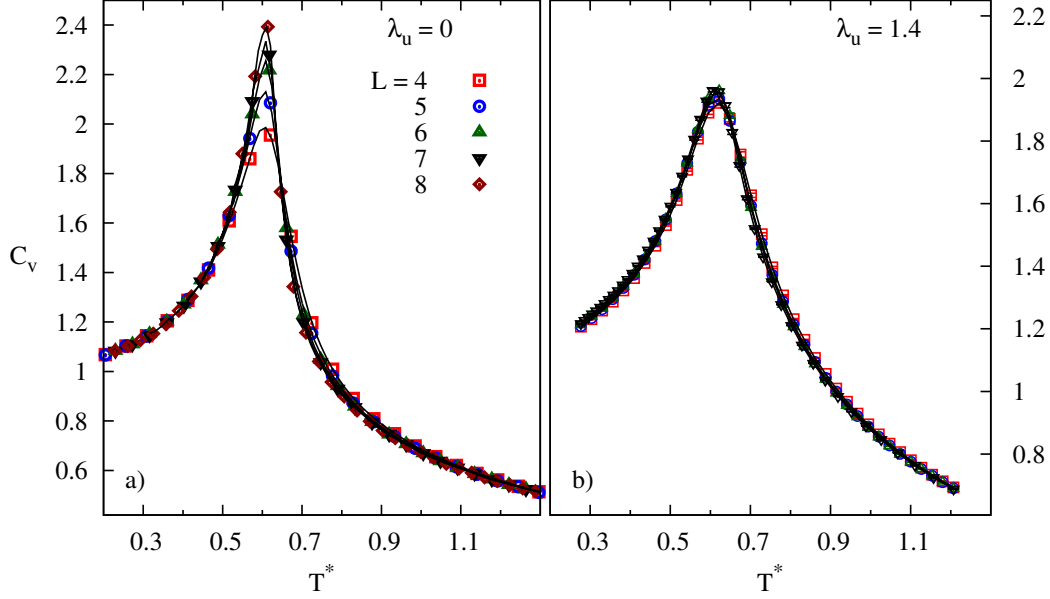


FIG. 5. Evolution of the heat capacity C_v with the system size L for a) the pure dipolar case ($\lambda_u = 0$) and $L = 4$ to 8 and b) $\lambda_u = 1.4$ and $L = 4$ to 7. The error bars are smaller than the size of the symbols. The lines result from the interpolation performed by the reweighting method⁴⁰.

we can get the variance σ of this distribution for a given value of P_2 . For instance at $T^* = 0.1$, we get $\sigma = 0.226, 0.458$ and 0.656 for $\lambda_u = 0, 0.8$ and 1.2 where $P_2 = 0.859, 0.543$ and 0.304 respectively. Then, at $\lambda_u = 1.2$, the value taken by B_m at low temperature is slightly smaller than 1, and the clear crossing observed for $T^* < T_c^*$ at lower values of λ_u becomes merely a merging at least for sufficiently large values of L . At $\lambda_u = 1.3$ the different $B_m(L)$ curves merge in a very limited range of temperature, and from $\lambda_u = 1.4$ and beyond $B_m(L)$ is a decreasing function of L whatever the value of T^* indicating the absence of PM/FM transition as displayed in figure (4 e,f). This is an indication of the change in the nature of the transition from the PM/FM to the PM/SG one or at least to a PM/glassy phase. This is corroborated by the reduction of the finite size dependence of the heat capacity, as can be seen on figure (5b), since no singular finite size behavior of C_v is expected in a PM/SG transition⁵². This latter feature is more evident on the dipolar component of C_v in the strong MAE coupling case (discussed in more detail in section III C and in figure (11)). We conclude that the PM/FM line extends from $\lambda_u = 0$ to $\lambda_u^{(s)} = 1.3$ and we expect the low temperature phase to present a SG character beyond this value.

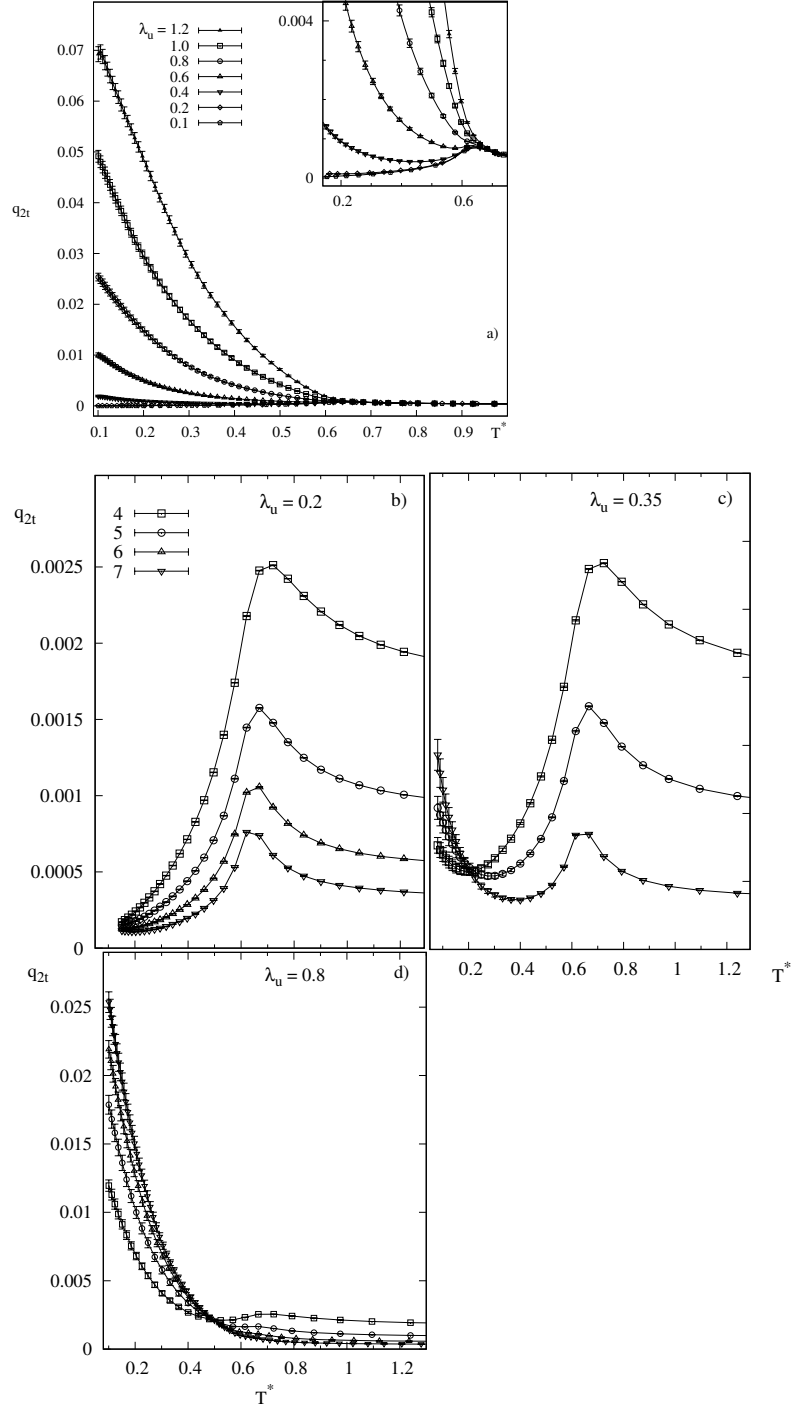


FIG. 6. Spin-glass transverse overlap order parameter defined in the plane normal to the nematic direction for a) $\lambda_u = 0.1$ to 1.2 as indicated and $L = 7$. Inset: detail of the hump in the vicinity of the PM/FM transition temperature. q_{2t} for $\lambda_u = 0.1$ and 0.2 are only slightly distinguishable at the scale of the inset. Finite size effect on q_{2t} , for $L = 4$ to 7 as indicated and b) $\lambda_u = 0.2$, c) $\lambda_u = 0.35$ showing the very beginning of the low temperature rising up in the latter case. d) Case $\lambda_u = 0.8$, well inside the QLRO region of the phase diagram.

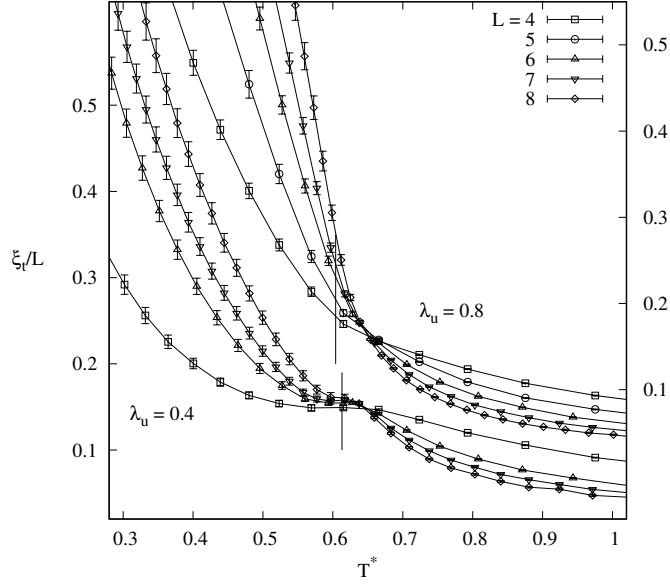


FIG. 7. Transverse spin-glass correlation length reduced by L for $\lambda_u = 0.4$, bottom and 0.8, top, showing the crossing point behavior in terms of T^* for different values of L . The vertical lines visualize the value of the PM/FM transition temperature T_c^* obtained from B_m .

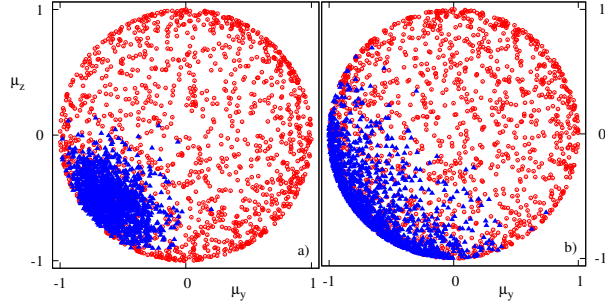


FIG. 8. Examples of the instantaneous moments distribution (μ_y, μ_z) at $T^* = 0.1$, solid triangles and in the PM phase, open circles for $\lambda_u = 0$, a) and 0.8, b).

B. Spin-glass transition

Beyond $\lambda_u = 1.4$ we are clearly in the PM/SG transition region. As is the case for the PM / chiral glass transition of the 3D Heisenberg spin-glass model the Binder cumulant (7) does not present a well defined crossing point as in the FM/PM transition. It is instead characterized by a dip in the B_q negative region, which deepens with the increase of L . The location of this dip must converge towards T_c^* ^{43,53,54}. Our simulations confirm such a behavior for B_q as can be seen in figure (9) where B_q is displayed for $\lambda_u = 4$. Therefore, for $\lambda_u > 1.5$, we determine the value of T_c^* as the crossing point of the ξ/L curves for different values of L on the one hand and the interpolation to $1/L = 0$ of the

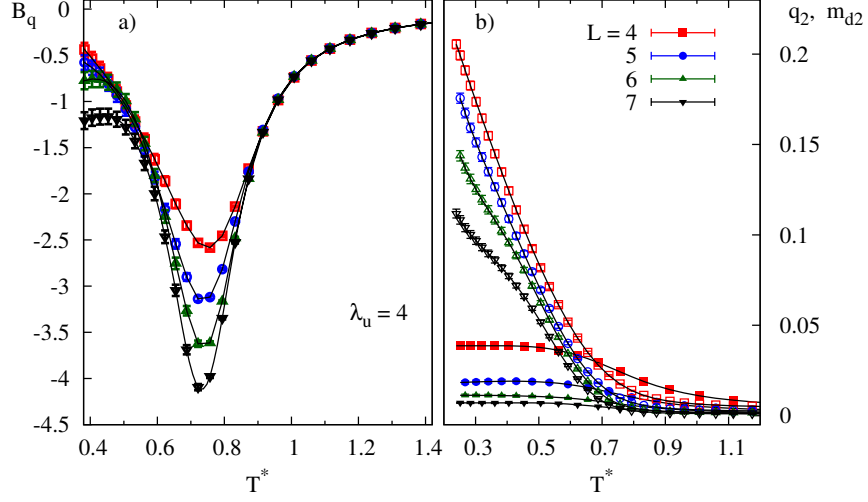


FIG. 9. Spin glass Binder cumulant B_q , a) and second moment of the spin-glass overlap order parameter, q_2 , open symbols, and of the magnetization, m_{d2} , solid symbols, b), for $\lambda_u = 4$ in terms of the system size L .

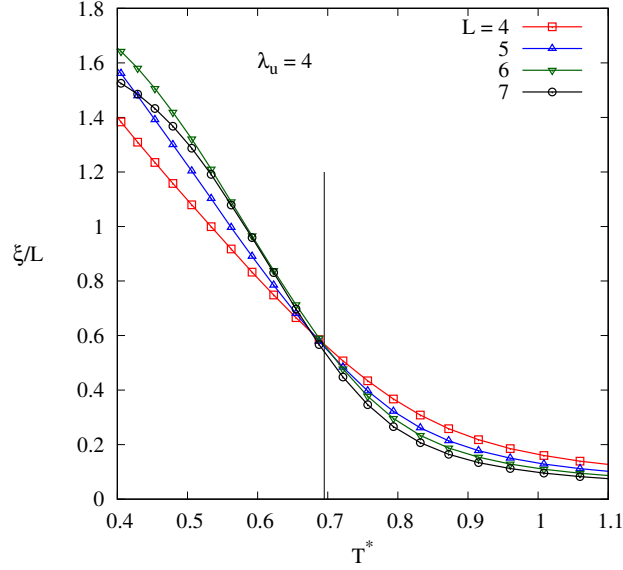


FIG. 10. Spin glass correlation length reduced by the system size in terms of T^* for $\lambda_u = 4$. The vertical line indicates the value of T_c^* obtained from the interpolation at $1/L = 0$ of the linear fit in terms of $1/L$ of the Binder cumulant dip temperature.

linear fit in $1/L$ of the value of T^* at the dip in B_q on the other hand. Because of the heaviness of the computations, we consider only $\lambda_u = 1.6, 2$ and 4 . The two above mentioned determinations of T_c^* are in quite good agreement, as can be seen in figure (10) corresponding to $\lambda_u = 4$. Furthermore the value of T_c^* in the limiting case, $\lambda_u \rightarrow \infty$, which is the so-called random axes dipoles (RAD) model^{55,56} is known from the literature, $T_c^*(\infty) = 0.95 \pm 0.05$ ²⁶.

The FM/SG transition line below T_c^* is not easy to locate. We have nevertheless estimated $\lambda_u(T_c^*)$ along the

FM/SG line from the condition that $B_m(L)$ at T^* constant is an increasing (decreasing) function of the system size L in the FM (SG) side of this line, with however a rather large uncertainty (see figure (1)).

C. Large λ_u limit

In the strong λ_u limit, the MAE contribution to the total Hamiltonian (1) tends to align the moments $\hat{\mu}_i$ on the anisotropy axes \hat{n}_i making the model coincide with the dipolar Ising model^{38,46,55,56}, the anisotropy axes playing the role of the Ising axes. In this limit as is the case for the $D/J \rightarrow \infty$ of the Heisenberg RAM²⁸, one is left with a much simpler system since the continuous 3D unit vector per site transforms in the two valued scalar variable of the Ising model. Therefore, it is important to determine the value of λ_u beyond which the system behaves as a dipolar Ising system. To do this we note that when $\lambda_u \gg 1$ the moments directions $\hat{\mu}_i$ get close to the axes \hat{n}_i leading to $\hat{\mu}_i \simeq s_i \hat{n}_i$ with $s_i = \pm 1$ and thus the Hamiltonian from equation (2b) can be written as

$$\beta H = \frac{1}{T^*} \left((1/2) \sum_{i \neq j} s_i J_{ij} s_j - \lambda_u \sum_i (\hat{\mu}_i \cdot \hat{n}_i)^2 \right) \quad (11)$$

Where J_{ij} are the coupling constants $\hat{n}_i \bar{T}_{ij} \hat{n}_j$, independent of the configuration of the moments $\{\hat{\mu}_i\}$ in the framework of the frozen easy axes distribution. Equation (11) reflects the fact that in this limit the MAE depends on the fluctuations $((\hat{\mu}_i \cdot \hat{n}_i)^2 - 1)$ conversely to the DDI which depends on the configuration of the $\{s_i\}$. We then have two independent sets of variables per site namely $\{s_i\}$ and $(\hat{\mu}_i \cdot \hat{n}_i)^2$. The second one, describing the MAE are totally uncoupled and represent two degrees of freedom per site ($\hat{\mu}_i$ are 3-dimensional unit vectors) and thus contribute, according to the Dulong and Petit law, or equivalently to the equipartition of energy, as Nk_B to the total heat capacity, or in other words ($C = C_v/(Nk_B)$)

$$C_{an}(T) = \frac{1}{Nk_B} \frac{d[\langle E_{an} \rangle]}{dT} \rightarrow 1 \quad (12)$$

Then equation (12) is a clear criterion to determine whether the system of interacting dipoles plus MAE is Ising like since it is an indication that the variables $\{s_i\}$ and $(\hat{\mu}_i \cdot \hat{n}_i)^2$ become uncoupled and equation (11) holds. In such a case, we expect the dipolar component of C , C_{dip} to be close to the C of the corresponding dipolar Ising model which does not include the component C_{an} , as for instance in the RAD case. From the heat capacity curves displayed in figure (11) we conclude that the Ising dipolar behavior is reached beyond $\lambda_u = 30$. It is worth mentioning that a similar conclusion was obtained in the case of the totally textured distribution of easy axes²⁶.

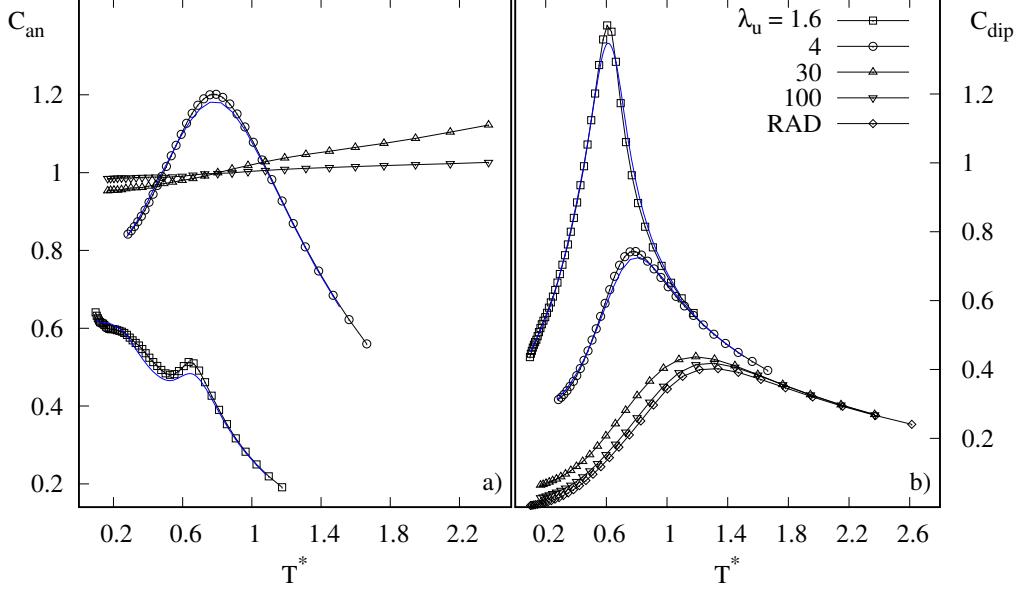


FIG. 11. Anisotropy, a) and dipolar, b) components of the heat capacity. In the RAD case the total capacity includes only the C_{dip} component. Symbol: $L = 7$ for $\lambda_u \leq 4$ and $L = 4$ otherwise. Solid blue lines for $\lambda_u \leq 4$: $L = 4$.

IV. CONCLUSION

In this work, we have determined a significant part of the magnetic phase diagram of an ensemble of dipoles with uniaxial anisotropy located on the nodes of a FCC lattice from tempered Monte Carlo simulations. This is motivated first by the search for the conditions under which a super-ferromagnetic phase induced by DDI can be reached in the supra-crystals of MNP synthesized experimentally, and more generally by the determination of the nature of the ordered low temperature phase in these systems. The nature of the low temperature ordered phase is found successively FM and SG with increasing the MAE strength. From the behavior of m_2 with respect to L at low T^* beyond $\lambda_u = 0.4$ we interpret the FM phase in this region of the phase diagram as a FM-QLRO phase. Moreover the FM-QLRO phase is related to a transverse spin-glass state.

The crucial points to relate our findings to actual experimental situations is to determine the corresponding value of the λ_u parameter and the reference temperature T_r defined as $T^* = T/T_r$ (see section II). λ_u and T_r are related to the physical characteristics of the MNP, the uniaxial anisotropy constant K and the saturation magnetization M_s by $\lambda_u = (24/\mu_0)(K/M_s^2)(\Phi_r/\Phi)$ and $T_r = \mu_0/(4\pi k_B)(\pi/6 M_s)^2 d^3(\Phi/\Phi_r)$ respectively from the definitions given after equations (1,2a). As typical examples, in the case of maghemite or cobalt MNP we get a lower bound $\lambda_u > 5$ which means that in the absence of texturation of the easy axes, the corresponding supra-crystals are in the SG region of the phase diagram at low temperature. A precise determination of T_r and thus of the transition temperature $T_c = T_c^* T_r$ necessitates the precise knowledge of both the MNP size d and M_s which because of finite size and surface chemistry effects deviates from its bulk value, making thus T_r specific to a given system, and not only to a given material. One

may also wonder on the effect of the temperature dependence of the relevant experimental parameters, M_s and K on the validity of such a model. Concerning M_s one has to keep in mind that the ordering temperature (either the Néel or the Curie temperature) of the usual MNP materials (*c.a.* $\sim 850 - 1000$ K) is much larger than the room temperature which is somewhat an upper bound for the MNP properties of interest and thus only a very small variation of M_s ($\sim M_s(0)(1 - (T/T_c))^b$, $b \sim 3/2$) is expected. Concerning K , since it is in general an effective anisotropy constant including different contributions (magnetocrystalline, shape, surface chemistry), a precise evaluation of $K(T)$ is not a simple task. However, our results show only a very weak dependence of the transition temperature with respect to λ_u . On an other hand an important bound is the T_b/T_r ratio, where T_b is the blocking temperature related to the MAE through $T_b = K v(d)/(ck_B)$, the constant c being specific to the measurement considered ($c \simeq 30$ for magnetometry). Below T_b the moments are blocked in the MAE potential well during the measurement and thus the DDI induced transition can be observed only if $T_b < T_r T_c^*$. From the definition of T_b we easily get $T_b/T_r = \lambda_u/c$ and consequently the DDI induced transition will be experimentally observable only if $\lambda_u < c T_c^*$, the sufficient condition being in any case $\lambda_u < c/2$ according to our results.

Finally, we also have obtained the limiting value beyond which the DDI plus uniaxial MAE model is assimilable to a 1D dipolar Ising model. This value, $\lambda_u \simeq 30$, seems larger than the experimental expectation of λ_u . As a result, modeling the MNP ensemble by a dipolar Ising model may be not strictly speaking justified.

V. ACKNOWLEDGEMENTS.

This work was granted an access to the HPC resources of CINES under the allocations 2018-A0040906180 and 2019-A0060906180 made by GENCI, CINES, France. We thank the SCBI at University of Málaga and IC1 at University of Granada for generous allocations of computer time. J.-J. A. thanks for financial support from grant FIS2017-84256-P (FEDER funds) from the Agencia Española de Investigación.

-
- ¹ Q. Pankhurst, N. Thanh, S. K. Jones, and J. Dobson, *J. Phys. D* **42**, 224001 (2009).
- ² C. Garnero, M. Lepasant, C. Garcia-Marcelot, Y. Shin, C. Meny, P. Farger, B. Warot-Fonrose, R. Arenal, G. Viau, K. Soulan-tica, P. Fau, P. Poveda, L.-M. Lacroix, and B. Chaudret, *Nano Letters* **19**, 1379 (2019).
- ³ A. Dreyer, A. Feld, A. Kornowski, E. Yilmaz, H. Noei, A. Meyer, T. Krekeler, C. Jiao, A. Stierle, V. Abetz, H. Weller, , and G. Schneider, *Nature Mat.* **15**, 522 (2016).
- ⁴ B. Domenech, A. Plunkett, M. Kampfbeck, M. Blankenburg, B. Bor, D. Giuntini, T. Krekeler, M. Wagstaffe, H. Noei, A. Stierle, M. Ritter, M. Muller, T. Vossmeier, H. Weller, and G. Schneider, *Langmuir* **35**, 13893 (2019).
- ⁵ S. Bedanta and W. Kleemann, *J. Phys. D* **42**, 013001 (2009).
- ⁶ S. Bedanta, A. Barman, W. Kleemann, O. Petravic, and T. Seki, *J. of Nanomaterials* **2013**, 952540 (2013).
- ⁷ W. Kleemann, O. Petravic, C. Binek, G. N. Kakazei, Y. G. Pogorelov, J. B. Sousa, S. Cardoso, and P. P. Freitas, *Phys. Rev. B* **63**, 134423 (2001).
- ⁸ O. Petravic, *Superlattices and Microstructures* **47**, 569 (2010).
- ⁹ J. A. De-Toro, S. S. Lee, D. Salazar, J. L. Cheong, P. S. Normile, P. Muniz, J. M. Riveiro, M. Hillenkamp, F. Tournus, A. Tamion, and P. Nordblad, *Appl. Phys. Lett.* **102**, 183104 (2013).
- ¹⁰ J. A. De-Toro, P. S. Normile, S. S. Lee, D. Salazar, J. L. Cheong, P. Muniz, J. M. Riveiro, M. Hillenkamp, F. Tournus, A. Tamion, and P. Nordblad, *J. Phys. Chem. C* **117**, 10213 (2013).
- ¹¹ E. Josten, E. Wetterskog, A. Glavic, P. Boesecke, A. Feoktystov, E. Brauweiler-Reuters, U. Rücker, G. Salazar-Alvarez, T. Brückel, and L. Bergström, *Scientific Reports* **7**, 2802 (2017).
- ¹² O. Kasyutich, A. Sarua, and W. Schwarzacher, *J. Phys. D* **41**, 134022 (2008).
- ¹³ O. Kasyutich, R. D. Desautels, B. Southern, and J. van Lierop, *Phys. Rev. Lett.* **104**, 127205 (2010).
- ¹⁴ M. Kostianen, P. Ceci, M. Fornara, P. Hiekkataipale, O. Kasyutich, R. Nolte, J. Cornelissen, R. Desautels, and J. van Lierop, *ACS Nano* **5**, 6394 (2011).
- ¹⁵ I. Lisiecki, D. Parker, C. Salzemann, and M. P. Pileni, *Chem. Mater.* **19**, 4030 (2007).
- ¹⁶ M. S. Andersson, R. Mathieu, S. Lee, P. S. Normile, G. Singh, P. Nordblad, and J. A. De-Toro, *Nanotechnology* **26**, 475703 (2015).
- ¹⁷ D. Mishra, M. Benitez, O. Petravic, G. B. Confalonieri, P. Szary, F. Brüsing, K. Theis-Bröhl, A. Devishvili, A. Vorobiev, O. Konovalov, M. Paulus, C. Sternemann, B. Toperverg, and H. Zabel, *Nanotechnology* **23**, 055707 (2012).
- ¹⁸ H. Kachkachi and E. Bonet, *Phys. Rev. B* **73**, 224402 (2006).
- ¹⁹ M. Vasilakaki, G. Margaris, D. Peddis, R. Mathieu, N. Yaacoub, D. Fiorani, and K. Trohidou, *Phys. Rev. B* **97**, 094413 (2018).
- ²⁰ J. P. Bouchaud and P. G. Zerah, *Phys. Rev. B* **47**, 9095 (1993).
- ²¹ J.-J. Weis and D. Levesque, *Phys. Rev. E* **48**, 3728 (1993).
- ²² G. Ayton, M. Gingras, and G. N. Patey, *Phys. Rev. E* **56**, 562 (1997).
- ²³ J.-J. Weis, *J. Chem. Phys.* **123**, 044503 (2005).
- ²⁴ V. Russier and E. Ngo, *Condensed Matter Physics* **20**, 33703 (2017).
- ²⁵ J. J. Alonso, B. Allés, and V. Russier, *Phys. Rev. B* **100**, 134409 (2019), arXiv:1909.13573.
- ²⁶ V. Russier and J.-J. Alonso, *Journal of Physics: Condensed Matter* **32**, 135804 (2020).
- ²⁷ R. Harris, M. Plischke, and M.-J. Zuckermann, *Phys. Rev. Lett.* **31**, 160 (1973).
- ²⁸ A. Chakrabarti, *Phys. Rev. B* **36**, 5747 (1987).
- ²⁹ M. Itakura, *Phys. Rev. B* **68**, 100405 (2003).
- ³⁰ H.-M. Nguyen and P.-Y. Hsiao, *Appl. Phys. Lett.* **95**, 222508 (2009).
- ³¹ H.-M. Nguyen and P.-Y. Hsiao, *J. Appl. Phys.* **105**, 07E125 (2009).
- ³² A.-V. Bondarev, V.-V. Ozherelyev, I.-L. Bataronov, and Y.-V. Barmin, *Bulletin of the Russian Academy of Sciences. Physics* **75**, 1352 (2011).
- ³³ Introducing $d_r = d(\Phi_r/\Phi)^{1/3}$ involving the volume fraction Φ of the system $((N/V)\pi d^3/6)$ and a reference value, Φ_r (for instance the maximum value for hard spheres on a FCC lattice), $(1/N)\sum_{i\neq j}^N(1/(r_{ij}/d_r)^3) = f(N)$ is found nearly independent of both the underlying structure and ϕ . As a result $(1/N)\sum_{i\neq j}^N([\hat{\mu}_i \cdot \hat{\mu}_j - 3(\hat{\mu}_i \cdot \hat{r}_{ij})(\hat{\mu}_j \cdot \hat{r}_{ij})]/(r_{ij}/d)^3)$ in equation (1)

is rewritten as $(\Phi/\Phi_r)(1/N) \sum_{i \neq j}^N ([\hat{\mu}_i \cdot \hat{\mu}_j - 3(\hat{\mu}_i \cdot \hat{r}_{ij})(\hat{\mu}_j \cdot \hat{r}_{ij})]/(r_{ij}/d_r)^3)$. Accordingly, $(\epsilon_d/k_B)(\Phi/\Phi_r)$ is a convenient measure of the temperature for this system from which our definition of T^* , $T^* = k_B T / (\epsilon_d(\Phi/\Phi_r))$ follows.

- ³⁴ M. P. Allen and D. J. Tildesley, “Computer simulation of liquids,” (Oxford Science Publications, 1987).
- ³⁵ P. G. Kusalik, *J. Chem. Phys.* **93**, 3520 (1990).
- ³⁶ K. Hukushima and K. Nemoto, *J. Phys. Soc. Japan* **65**, 1604 (1996).
- ³⁷ D.-J. Earl and M.-W. Deema, *Phys. Chem. Chem. Phys.* **7**, 3910 (2005).
- ³⁸ J. J. Alonso and J. F. Fernández, *Phys. Rev. B* **81**, 064408 (2010).
- ³⁹ D. Sabo, M. Meuwly, D. Freeman, and J. Doll, *J. Chem. Phys.* **128**, 174109 (2008).
- ⁴⁰ A. Ferrenberg and R. Swendsen, *Phys. Rev. Lett.* **61**, 2635 (1988).
- ⁴¹ K. Binder, *Phys. Rev. Lett.* **47**, 693 (1982).
- ⁴² L. A. Fernandez, V. Martin-Mayor, S. Perez-Gaviro, A. Tarancon, and A. P. Young, *Phys. Rev. B* **80**, 024422 (2009).
- ⁴³ D. X. Viet and H. Kawamura, *Phys. Rev. Lett.* **102**, 027202 (2009).
- ⁴⁴ F. Cooper, B. Freedman, and D. Preston, *Nucl. Phys. B* **210**, 210 (1982).
- ⁴⁵ H. Ballesteros, L. Fernández, V. Martín-Mayor, J. Pech, J. J. Ruiz-Lorenzo, A. Tarancón, P. Téllez, C. L. Ullod, and C. Ungil, *Phys. Rev. B* **62**, 14237 (2000).
- ⁴⁶ A. Klopper, U. Roßler, and R. Stamps, *Eur. Phys. J. B* **50**, 45 (2006).
- ⁴⁷ B. Alkadour, J.-I. Mercer, J.-P. Whitehead, B.-W. Southern, and J. van Lierop, *Phys. Rev. B* **95**, 214407 (2017).
- ⁴⁸ A.-D. Bruce and A. Aharony, *Phys. Rev. B* **10**, 2078 (1974).
- ⁴⁹ T. Papakonstantinou, N. G. Fytas, A. Malakis, and I. Lelidis, *Eur. Phys. J. B* **88**, 94 (2015).
- ⁵⁰ We do not expect C_v to diverge at the transition because of the scaling relation, $\alpha = 2 - 3\nu$ in 3D and according to $(C_v^*(L) \sim C_v^*(\infty) - bL^{\alpha/\nu})$ since in any case we do not expect $\nu < 2/3$ in our system.
- ⁵¹ A. D. Beath and D. H. Ryan, *Phys. Rev. B* **76**, 064410 (2007).
- ⁵² A. T. Ogielski, *Phys. Rev. B* **32**, 7384 (1985).
- ⁵³ D. X. Viet and H. Kawamura, *Phys. Rev. B* **80**, 064418 (2009).
- ⁵⁴ T. Ogawa, K. Uematsu, and H. Kawamura, *Phys. Rev. B* **101**, 014434 (2020).
- ⁵⁵ J. Fernández and J. J. Alonso, *Phys. Rev. B* **79**, 214424 (2009).
- ⁵⁶ J. J. Alonso and B. Allés, *J. Phys. Condens. Matter* **29**, 355802 (2017).